NANO · MICRO small
www.small-journal.com

Hierarchical Synergistic Structure for High Resolution Strain Sensor with Wide Working Range

Runhui Zhou, Yufei Zhang, Fan Xu, Zhuoyu Song, Jiaoya Huang, Zemin Li, Chen Gao, Jiang He, Wenchao Gao,* and Caofeng Pan**

Strain sensors have been attracting tremendous attention for the promising application of wearable devices in recent years. However, the trade-off between high resolution, high sensitivity, and broad detection range is a great challenge for the application of strain sensors. Herein, a novel design of hierarchical synergistic structure (HSS) of Au micro cracks and carbon black (CB) nanoparticles is reported to overcome this challenge. The strain sensor based on the designed HSS exhibit high sensitivity (GF > 2400), high strain resolution (0.2%) even under large loading strain, broad detection range (>40%), outstanding stability (>12000 cycles), and fast response speed simultaneously. Further, the experiments and simulation results demonstrate that the carbon black layer greatly changed the morphology of Au micro-cracks, forming a hierarchical structure of micro-scale Au cracks and nano-scale carbon black particles, thus enabling synergistic effect and the double conductive network of Au micro-cracks and CB nanoparticles. Based on the excellent performance, the sensor is successfully applied to monitoring tiny signals of the carotid pulse during body movement, which illustrates the great potential in the application of health monitoring, human-machine interface, human motion detection, and electronic skin.

1. Introduction

With the development of technology, wearable devices for personal healthcare, human-machine interface, and robotics possess enormous prospects.[1–3] Strain sensors with excellent performance in sensing mechanical stimuli, as a vital component of wearable devices, have attracted tremendous attention in recent years. The human body provides abundant strain signals induced by human posture, activity, and various biosignals that can be detected by strain sensors for the application of health monitoring. Hence, high sensitivity was required to detect tiny motions including heartbeat, phonation, and respiration. While in actual application, the tiny strain signals of health monitoring are normally accompanied by large strain induced by body movements, which request broad detection range, high sensitivity, and high strain resolution to ensure intact functionality under different strain levels. However, the present strain sensors generally possess only one feature mentioned above, either high sensitivity with a narrow detection range or broad detection range with low sensitivity, meanwhile, high strain resolution was rarely studied in flexible strain sensors.

The high sensitivity of strain sensors is normally related to large structural changes under strain causing drastic conductance change, such as crack based strain sensors. Conventional highly sensitive crack based strain sensors were mostly based on brittle metal films which intended to generate cracks under strain to release energy.[4] The sensing mechanism of crack-based strain sensors is based on reversible separation and connection of cracks, which causes dramatic resistance change under strain, enabling the crack-based strain sensors with high sensitivity but narrow detection range normally below 5% strain. As one of the most influential works of

R. Zhou, Y. Zhang, F. Xu, J. He, W. Gao, C. Pan
CAS Center for Excellence in Nanoscience
Beijing Key Laboratory of Micro-nano Energy and Sensor
Beijing Institute of Nanoenergy and Nanosystems
Chinese Academy of Sciences
101400 Beijing, P. R. China
E-mail: hejiang@binn.cas.cn; gaowenchao@binn.cas.cn; cfpan@binn.cas.cn

R. Zhou, F. Xu, C. Pan
School of Nanoscience and Engineering
University of Chinese Academy of Sciences
100049 Beijing, P. R. China

Z. Song
Department of Engineering Mechanics
Dalian University of Technology
Dalian, Liaoning 116024, China

J. Huang, C. Pan
Center on Nanoenergy Research
School of Physical Science and Technology
Guangxi University
Nanning, Guangxi 530004, P. R. China

Z. Li
School of Chemistry and Chemical Engineering
Guangxi University
Nanning, Guangxi 530004, P. R. China

C. Gao
School of Physics
University of Chinese Academy of Sciences
100049 Beijing, P. R. China

The ORCID identification number(s) for the author(s) of this article can be found under https://doi.org/10.1002/smll.202301544

DOI: 10.1002/smll.202301544

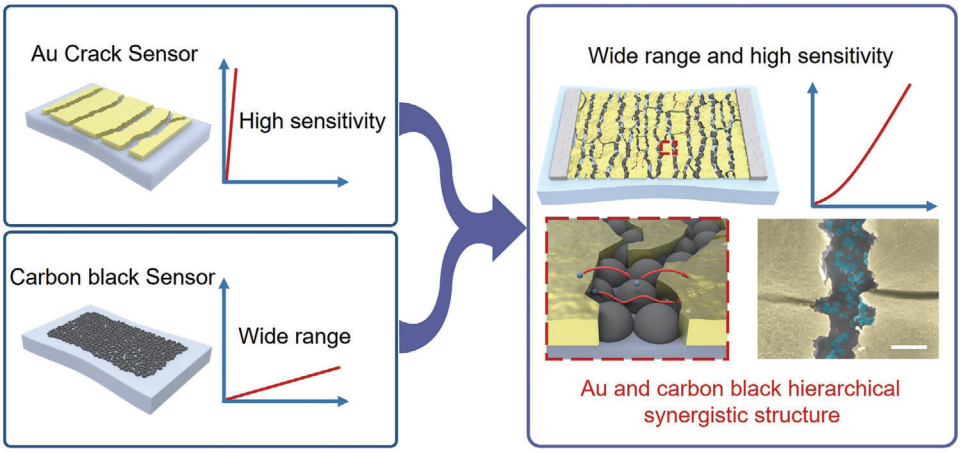

Figure 1. Illustration of Au and CB double conductive network hierarchical synergistic structure based strain sensor design concept and fabrication. The scale bar is 500 nm.

crack-based strain sensors, Daeshik et. al. reported a spider-like crack-based strain sensor, which was prepared by depositing platinum on PUA substrate.[5] The spider-like strain sensor possessed a high gauge factor of 2000 and a sensing range of 2%. Further, the gauge factor of the crack-based sensor was improved to 16 000 by modulating crack depth.[6] Despite the high sensitivity of crack-based strain sensors, the narrow detection range greatly limits the applications. Hence many efforts have been made in modifying the materials[5–7] and structures[8] of sensing films and engineering crack structures such as crack density,[9] crack depth,[6] crack connection,[10,11] and crack distribution[12] to enhance the sensing performance.

As for the broad detection range, in contrast, expanding the detection range requires small structure changes under strain to ensure the robustness of conductive paths. The strain sensors with broad detection range were normally prepared by mixing conductive fillers into polymer matrix to form a composite structure. Thus varied sensing materials have been reported including, metal nanomaterials (e.g., nanowires,[11,13] nanoflakes,[14] and nanoparticles[15,16]), carbon-based materials (e.g., carbon black (CB),[17–19] carbon nanotube (CNT)[20–23] and graphene (Gr),[24–26] MXenes,[27,28] ionic liquid,[29,30] liquid metal,[31] and conductive polymers.[32–34] Such structure maintain the robustness of conductive paths under large strain by diluting applied strain into tiny distance changes of conductive fillers, thus obtaining a broad detection range. Therefore, it normally exhibits low sensitivity. Accordingly, it is hard for a single structure to simultaneously meet the requirements of high strain resolution, high sensitivity, and broad detection range. The key point of simultaneously realizing the above-mentioned properties is to solve the contradiction between the need for large structural change and the need for small structural change under a large strain range.

Herein we designed a hierarchical synergistic structure of Au micro cracks and CB nanoparticles to surmount this obstacle (**Figure 1**). In order to combine these two microscales and nanoscale structures, we first prepared a highly uniform Langmuir monolayer film of CB through the interface self-assembly method. Then a thin layer of Au film was deposited on the CB film to construct a hierarchical synergistic structure with the double conductive network. The introduction of CB greatly changed the propagation of Au cracks and formed synergistic effect. The dense and twisty cracks of Au films induced by CB particles intended to separate under small strain, causing obvious resistance change. Additionally, the distance between CB nanoparticles further increased under large strain to alter conductive paths, enabling large detection range. Based on the synergistic effect of the hierarchical structure of Au micro cracks and CB nanoparticles, the resulting strain sensor obtained high gauge factor of 2420, high strain resolution (0.2%) even under large loading strain, and broad detection range of 45%. We further performed sound detection and long-term pulse monitoring based on our strain sensor, which illustrates the enormous potential in the application of healthcare and human-machine interfaces.

2. Results and Discussion

2.1. Fabrication and Characterization of HSS

The schematic illustration of the design concept of hierarchical synergistic structure (HSS) was shown in Figure 1, the main purpose was to form hierarchical synergistic effect by combining microscale crack structures with high sensitivity and nanoscale nanoparticle structures with large sensing ranges. Our method was coalescing Au film and CB film into a hierarchical synergistic structure. The hierarchical combination of microscale Au cracks and nanoscale CB particles with synergistic effect and double conductive network introduced by CB particles in the meantime enable the simultaneous realization of high sensitivity, large sensing range, and high strain resolution.

The fabrication process was illustrated in **Figure 2**a. The as-prepared CB dispersion was sprayed onto the surface of the water. With the increasing amount of CB dispersion sprayed onto the surface of the water, a highly uniform Langmuir monolayer film of loosely packed CB particles was formed under the Marangoni forces and airflow. Then a sponge was placed at the edge of the container to quickly siphon water. Subsequently, the highly uniform Langmuir monolayer become closely packed toward the opposite direction of the siphon direction. The photographs of

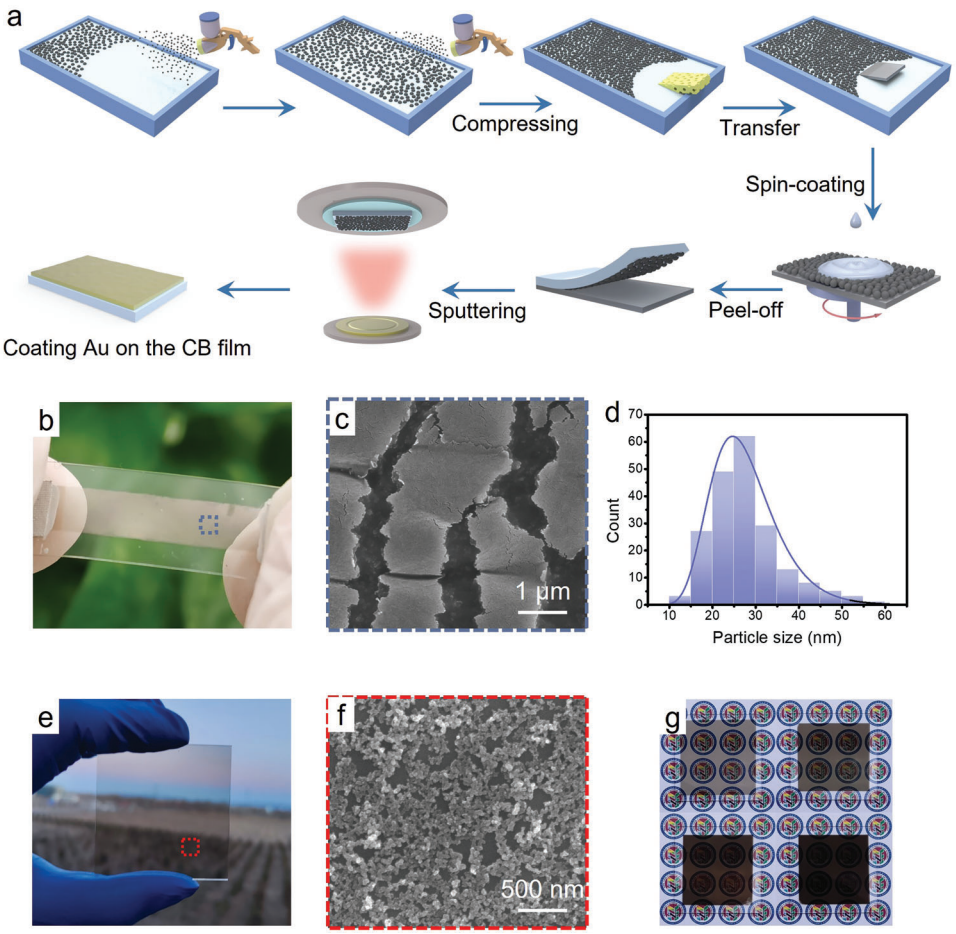

Figure 2. Fabrication and characterization of the HSS. a) The fabrication process of hierarchical synergistic structure of Au and CB. b) Photograph of the CB film after coating Au c) SEM imagines of CB-Au film under strain. d) size distribution of CB particles. e) Photograph of a single layer of self-assembled CB film transferred onto glass. f) SEM images of self-assembled CB film transferred onto silicon wafer. g) Photographs of different layers of self-assembled CB film.

different stages of fabrication of highly uniform monolayer CB films were shown in Figure S1 (Supporting Information). Then the closely packed highly uniform monolayer CB films were transferred to a polystyrene substrate or glass sheet. Next, PDMS was spin-coated on the CB films. After PDMS was cured, the PDMS-CB composite film was peeled off from the polystyrene substrate. Finally, a thin layer of gold was magnetron sputtered on the PDMS- CB composite film. The photograph of CB-Au composite films was shown in Figure 2b, and the SEM image was shown in Figure 2c suggesting the successful construction of a double conductive network hierarchical synergistic structure. In addition, the single layer of CB film transferred on the glass sheet was transparent and highly uniform as shown in Figure 2e. The SEM images in Figure 2f and Figure S2 (Supporting Information) suggest that the CB particles were uniformly dispersed without agglomeration. And the size distribution of CB particles was shown in Figure 2d, which was narrowly concentrated at 20–30 nm. Then multiple layers of CB films by repeating transferring process were prepared. Moreover, the uniformity of multilayer CB films was maintained after multiple transfer processes, as shown in Figure 2g and Figure S2 (Supporting Information). As the number of CB layers increases, the transparency of CB films decreases. The single layer of CB film possesses the highest transparency in these CB films of about 80% transmittance (Figure S3a, Supporting Information). Moreover, the resistance of CB film decreases with increasing CB layers, the average sheet resistance decreases from 182.9 ± 5.9 kΩ sq^{-1} to 29.9 ± 0.27 kΩ sq^{-1} when the number of layers increases from one to five layers (Figure S3b, Supporting Information). When the second layer of CB was transferred, the sheet resistance dropped rapidly because the voids of the first CB layer were mostly covered by the second CB layer. As shown in Figure S2 (Supporting Information), the voids were rare after more than two layers of CB particles.

2.2. Sensing Performance of HSS Based Strain Sensor

Then the self-assembled CB films with different layers were peeled off by PDMS and cut into the appropriate size to prepare into strain sensors. Then, the performance of the prepared strain sensor was tested. As the key parameters of strain sensors, the

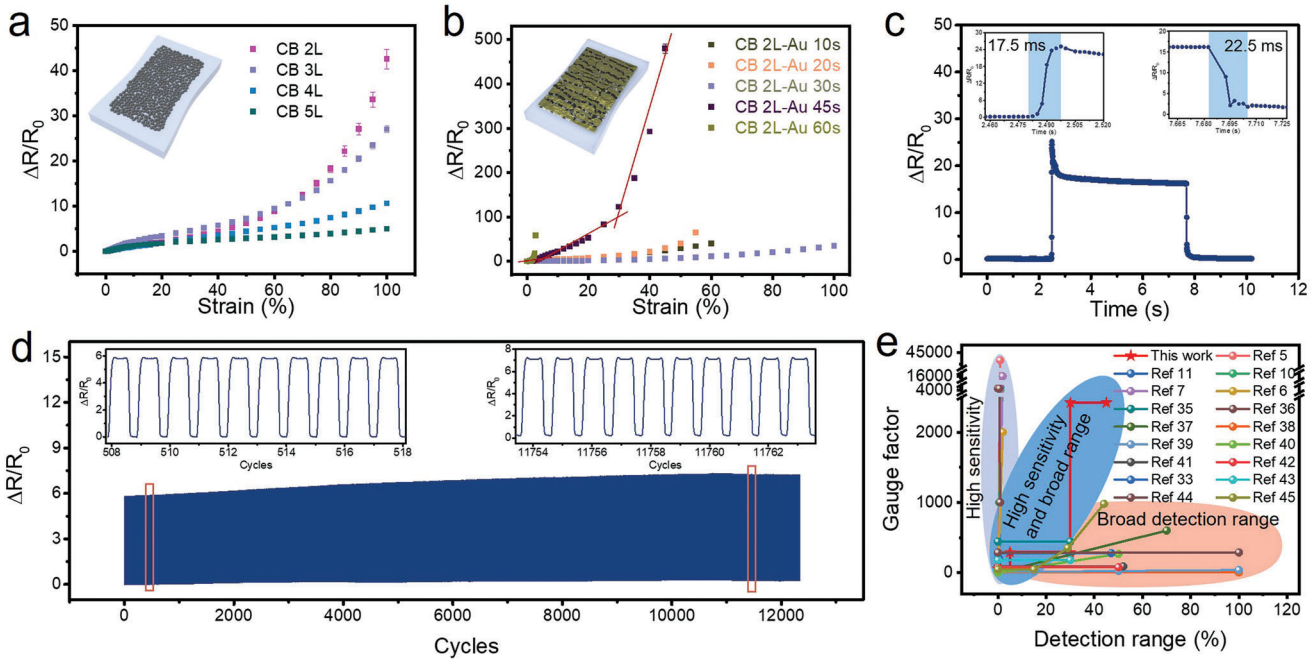

Figure 3. Sensing performance of the HSS based strain sensors. a) Relative resistance changes of strain sensors based on different layers of CB film under different strains. b) Relative resistance changes of strain sensors composed of two layers of CB film coated with Au by sputtering at different times under different strains. c) The response time and recovery time of the HSS based strain sensors. d) Long-term stability over 12 000 cycles. e) Comparison of sensing range and gauge factor with other papers.

sensitivity and detection range are vital properties of the sensors in actual applications. The sensitivity is normally evaluated by gauge factor (GF), which is defined as $GF = (\Delta R/R_0)/\epsilon$, where R_0 is the initial resistance of the strain sensor under a normal state, and ΔR is the change in resistance under applied strain ϵ. In order to optimize the performance of the strain sensor, the influence of the materials of the sensing layer was studied. First, the sensing performance of strain sensors based on different CB layers was studied. The experiment results manifested that the sensitivity decreases with increased numbers of CB layers (**Figure 3**a). The strain sensors based on double layers CB films exhibited the highest sensitivity, which possessed GF of 109 (at strain range of 80–100%). The sheet resistance of single-layer CB film after being peeled off by PDMS was too large to be applied in strain sensing, which was mainly attributed to the penetration of PDMS into the voids in the single CB layer. Subsequently, in order to balance sensitivity and sensing range, we propose a hierarchical synergistic structure by combining Au micro-crack layer and CB nanoparticles layer. Therefore, a thin layer of Au was magnetron sputtered on the double-layer CB films. In order to investigate the effect of the thickness of Au layer, the time of magnetron sputtering was precisely controlled. The CB-Au composite films with a sputtering time of 45s possessed the highest sensitivity (GF of 2420 at strain range of 30–45%) (Figure 3b), which might be due to that Au formed continuous film at a sputtering time of 45s (Figure S4, Supporting Information). Further, to confirm the required time of forming a continuous film of Au by sputtering, Au film with different times of magnetron sputtering was fabricated on a silicon wafer, and the Sputtered Au become a continuous film at a time of 45s (Figure S5, Supporting Information). Furthermore, our HSS based sensors exhibited fast response speed and excellent stability. Then, the response time and recovery time were measured (Figure 3c). The response time and recovery time were 17.5 ms and 22.5 ms, separately, and the fast response capability could enable high frequency detection. Next, the stability under different strains and different frequencies was studied, as shown in Figure S6a,b (Supporting Information). The multiple responses to different strains were nearly the same and the response barely changed with different frequencies. As in the actual application of human motion detection, thin features and long-term stability are vital parts. Therefore, the PDMS substrate with a thickness of 50 μm was prepared and used to peel off CB films. The long-term cyclic test was implemented based on HSS based sensors with 50 μm PDMS under 10% strain. The result in Figure 3d indicated excellent stability of our HSS based sensors that no obvious performance degradation was observed after over 12 000 cycles of stretching. In addition, the comprehensive performance was the state of art after comparison with other reported works (Figure 3e),[5–7,10,11,33,35–45] and the details of comparison were listed in the Table S1 and Note S1 (Supporting Information).

2.3. Sensing Mechanism Analysis of HSS Based Strain Sensor

In recent reports, the high sensitivity strain sensors were mostly based on the crack propagation mechanism which could achieve a sensitivity of over 10 000, while the sensing range was normally below 5% strain. Additionally, the strain sensors with a wide range were mainly based on the percolation theory that

distance changes between nano or micro conductive fillers induced by strain affect resistance. The vast amounts of nano or micro conductive fillers distribute strain which ensures the robustness of conductive paths, thus obtaining a wide sensing range. Meanwhile, high strain resolution was rarely studied in flexible strain sensors. The high strain resolution normally requires obvious structure changes under different strain levels. Therefore, the trade-off among sensitivity, strain resolution, and sensing range was difficult to overcome.

While the balance among sensitivity, strain resolution and sensing range were realized by the construction of the hierarchical structure and synergistic effect of Au micro crack and CB nanoparticles. The sensing mechanism was extensively studied. Firstly, the micro-morphology of Au film and CB-Au composite film with and without strain was investigated. A comparison of SEM images of gold film and CB-Au composite film was shown in **Figure 4**a,b. The results indicated that longer cracks were formed perpendicular to the stretching direction in Au films under a small strain of 5% resulting in a rapid increase in resistance, which was supported by previously reported strain sensors based on metal films including gold,[46] silver,[7] and platinum.[5,6] While the introduction of CB layers greatly changed the micro-morphology of cracks, that much shorter and denser twisty cracks were observed in CB-Au composite films under the same strain, as shown in Figure 4b. Moreover, the statistical analysis result of the crack length of the Au film and the CB-Au composite film was obtained that crack lengths were 56.35 μm and 8.12 μm, respectively, which signified that the crack length of the CB-Au composite film was much smaller than that of the Au film under the same strain (Figure 4e). These longer cracks in Au films normally cause greater resistance change.[42] In order to investigate the effect of the micro-morphology of cracks on electrical conductivity, we simulated the potential distribution of the SEM images by finite element analysis, according to the previous report.[42] The SEM images were imported into COMSOL after being turned into binary images, and the simulation was performed by applying a voltage across both sides. Figure 4c,d demonstrated that the potential distribution of CB-Au composite film dropped slower than that of the Au film, indicating larger strain tolerance in the CB-Au composite film. Furthermore, due to the vast amount of CB nanoparticles, the applied strain would be converted to the uniform displacement of CB nanoparticles as shown in Figure S8 (Supporting Information). The introduction of CB layers greatly changed the morphology and stress distribution on the surface. To understand the mechanism of the micro-morphology of CB-Au composite film under strain, we simulated the stress distribution of substrates with and without the CB layer. The simulation result, shown in Figure 4f, verified that the introduction of the CB layer enormously changed the stress distribution. The corresponding stress distribution map of PDMS with the CB layer showed that local stress near CB particles was obviously larger than other regions, in other words, the stress was substantially enhanced near CB particle regions. However, the stress distribution map of bare PDMS film showed that only a small region at the edge possessed larger stress, while the stress distribution in the central region is uniform. Moreover, we also conducted stress distribution simulations of 1D materials with different aspect ratios. As shown in Figure S9 (Supporting Information), the stress concentration was obviously enhanced as the aspect ratios decreased, indicating that the zero-dimensional materials like CB nanoparticles could better enhance the stress concentration (More details could refer to Note S2, Supporting Information). Additionally, the adhesion strength between gold and PDMS film was qualitatively investigated (More experiment details could refer to Movies S1 and S2, Supporting Information). Figures S10 and S11 (Supporting Information) demonstrated that the introduction of the CB layer considerably enhanced the adhesion strength between gold and CB-PDMS film, importantly, the interface toughness and the stress conduction to the metal film largely affect the morphology of cracks.[4,47] Consequently, the vast amount of CB particles introduced a vast amount of stress concentration site, meanwhile, Au as the intrinsic unstretchable material tends to form cracks under strain to release strain energy.[4] Thus, the dense short cracks were intended to propagate in CB-Au composite film. Furthermore, to better understand the interaction between the CB particles and Au film, the cracks generation of CB-Au hierarchical synergistic structure and Au film was simulated through finite element analysis (Figure S12, Movies S3 and Movie S4, Supporting Information), which revealed that cracks in the hierarchical synergistic structure possessed higher numbers and smaller lengths. Additionally, the CB particles generated significant stress concentration and the cracks in the CB-Au basically followed the stress concentration points created by CB particles, as shown in Figure S13 (Supporting Information) (More details could refer to Note S3, Supporting Information).

Further investigation of the micro-morphology of cracks in CB-Au composite revealed that CB particles were distributed between Au cracks, which suggests CB provided more effect than altering the micro-morphology of Au films. As shown in Figure 4g and Figure S14 (Supporting Information), under 50% strain CB particles were clearly observed between cracks, which suggests that CB particles could bridge Au cracks and provide robust conductive paths to realize a larger sensing range. Detail illustration of the mechanism was shown in Figure 4h. The changes in conductive paths of CB-Au composites and Au film under small strain and larger strains were illustrated. Under small strain, cracks of both CB-Au composites and Au film were intended to separate, causing great resistance change. With the increase of strain, longer cracks were formed in the Au film thus obstructing the conductive paths. However, the CB particles in CB-Au composites could bridge Au cracks to obtain extra conductive paths to possess a large sensing range, and due to the small amount of CB nanoparticles between cracks and the relatively poor conductivity of CB nanoparticles, the increase of strain can continue to change the distance between CB nanoparticles causing great resistance change under large strain level. Hence, the high sensitivity and high strain resolution were remained with large detection range.

2.4. Representative Applications for Small and High Frequency Vibration Detection

In order to simultaneously realize large human motion detection and small physiological signals monitoring, a large sensing range, and high sensitivity are required. Due to the excellent performance of our HSS based sensors, large signals of body movements and small biosignals of vibration induced by sound and

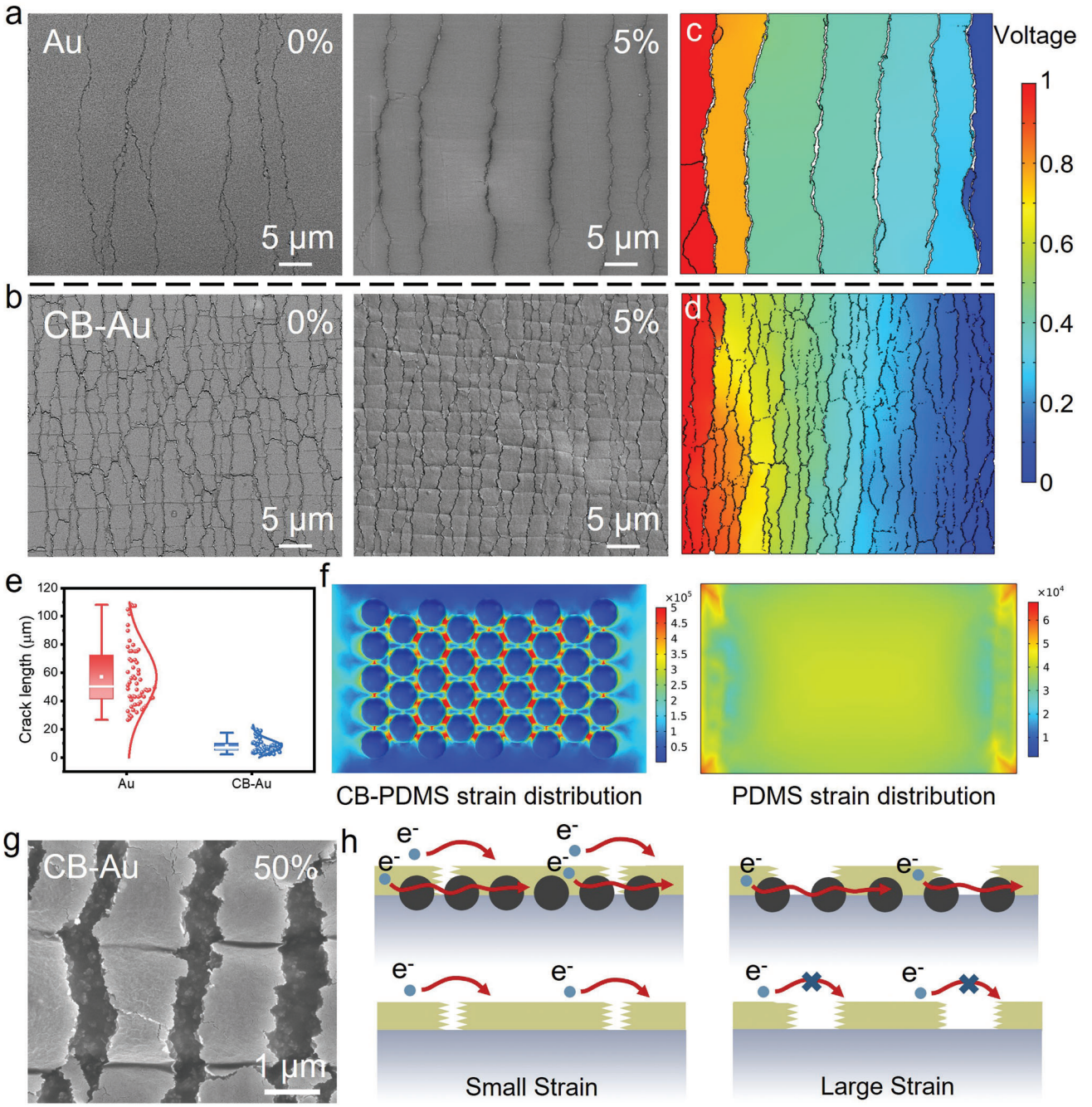

Figure 4. Crack morphology and strain distribution of strain sensor built from CB-Au film and gold film. a) SEM images of crack morphology of the gold film. b) SEM images of crack morphology of CB-Au film. c,d) Voltage distribution simulation based on SEM images of (a) and (b). e) Comparison of crack length of CB-Au film and gold film under the same strain. f) Strain distribution simulation of CB combined PDMS and flat PDMS. g) SEM images of crack morphology of CB-Au film under 50% strain. h) Schematic diagram of conductive path changes of HSS and Au film under small strain and large strain.

heartbeats were precisely detected simultaneously. Firstly, the application of HSS based sensors in small biosignal detection was performed. In order to ensure firmly conformal contact between sensors and human skin, the sensors were prepared based on the 50 μm PDMS and attached to a thin PU adhesive. Then our sensors were attached to the throat and the movement of muscles in the throat was accurately recorded, as shown in **Figure 5**a. Next, to exhibit the application of our sensors in high frequency small vibration detection scenarios, the response of our sensors to sound was tested by playing recordings of "BINN" and "sensor" through the speaker of a smartphone, and the responding data of our sensor was recorded by oscilloscope. The responding data was shown in the upper part of Figure 5b, and the spectral information was extracted through the STFT method and shown

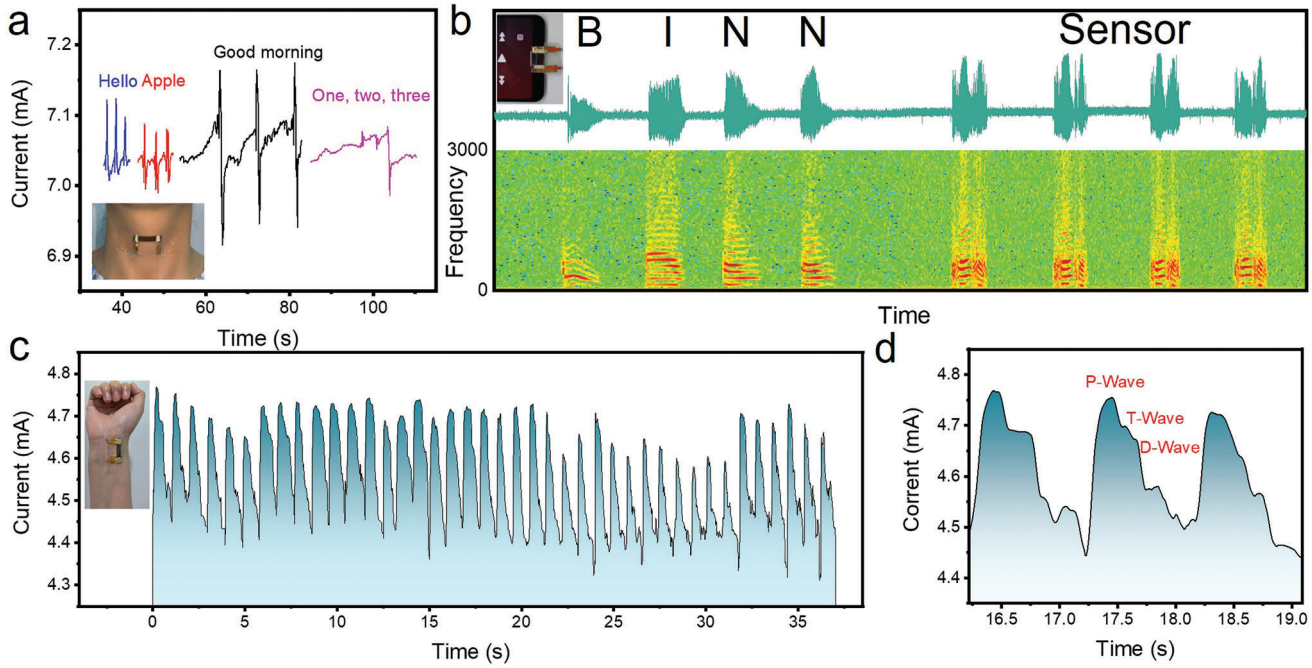

Figure 5. Application of strain sensor built from CB-Au film in small physiological signal detection. a) Resistance response to throat muscles movement when speaking. b) HSS based strain sensor response to Sound vibration and frequency spectrogram. c) Wrist pulse monitoring. d) Details of wrist pulse response curve.

in the lower part of Figure 5b, which illustrates potential applications in monitoring small vibrations related to human biosignals. Additionally, heartbeat is a weak signal and an important indicator of health status, which is an integral part of health monitoring. For the demonstration of the application of our HSS based sensors in health monitoring, a human pulse monitoring test was performed by attaching our sensor to the wrist and neck, which was shown in Figure 5c. The signals of wrist pulse were accurately and stably recorded, which provided vital information about heart condition. Importantly, three characteristic peaks of the human pulse waveform were clearly shown in Figure 5d, which contained the percussion wave (P-Wave), the tidal wave (T-Wave), and the diastolic wave (D-Wave).

2.5. High Strain Resolution Performance and Long-Term Health Monitoring

Additionally, apart from sensitivity and detection range, another key parameter of the strain sensor is strain resolution. The ideal strain sensor should be able to detect tiny strain signals under both small and large strain levels, as illustrated in **Figure 6**a. In actual applications, the tiny strain signals are usually accompanied by large strain induced by body movements of tested position, hence the high strain resolution under both small and large strains is essential. Therefore, the sensing performance of our HSS based sensors to tiny strain under large strain levels was tested. During the test, the strain of 5% was first applied to our strain sensor at the consecutive step of strain of 1%. After the strain level reached 5%, the successive step of strain of 0.2% was applied. Then, the same procedures were performed at strain levels of 10% and 15%. The corresponding current changes of our device under constant potential were measured throughout the testing process and presented in Figure 6b. The result showed that each strain increment successfully leads to the stepped decrement of current with a swift and steady response, which demonstrated the excellent strain resolution of our HSS based sensors. In order to further quantitative analysis of the strain resolution of our device, the relative current changes of each strain step of 0.2% under different strain levels were obtained and the statistical analysis result was shown in Figure 6c. The response data of relative current changes of each strain step were all distributed in a very concentrated range, additionally, the response data of each strain step could be evidently distinguished from each other, all of which demonstrated the prominent strain resolution of our device. Furthermore, to quantify the concentration of the response data of each strain step, we calculated the coefficient of variation of the response data, which was used to differentiate the measures of dispersion of data. The coefficient of variation is defined as $CV = \sigma/\mu$, where CV is the coefficient of variation, σ is the standard deviation, and μ is the average value. As shown in Figure S7 (Supporting Information), the coefficient of variation was all around 0.04, with only one data group at strain level of 15%, ≈0.15 which was also small.

For long-term health monitoring, it is uncomfortable and difficult to let monitored person remain stationary for a long period. Hence, the tiny strain signals induced by physiological signals like pulse would be easily immersed in large body movement signals. However, normal strain sensors with highly sensitive or broad sensing range often suffer from small sensing or low sensitivity respectively, which cannot satisfy the requirements of measuring tiny strain and large strain signals at the

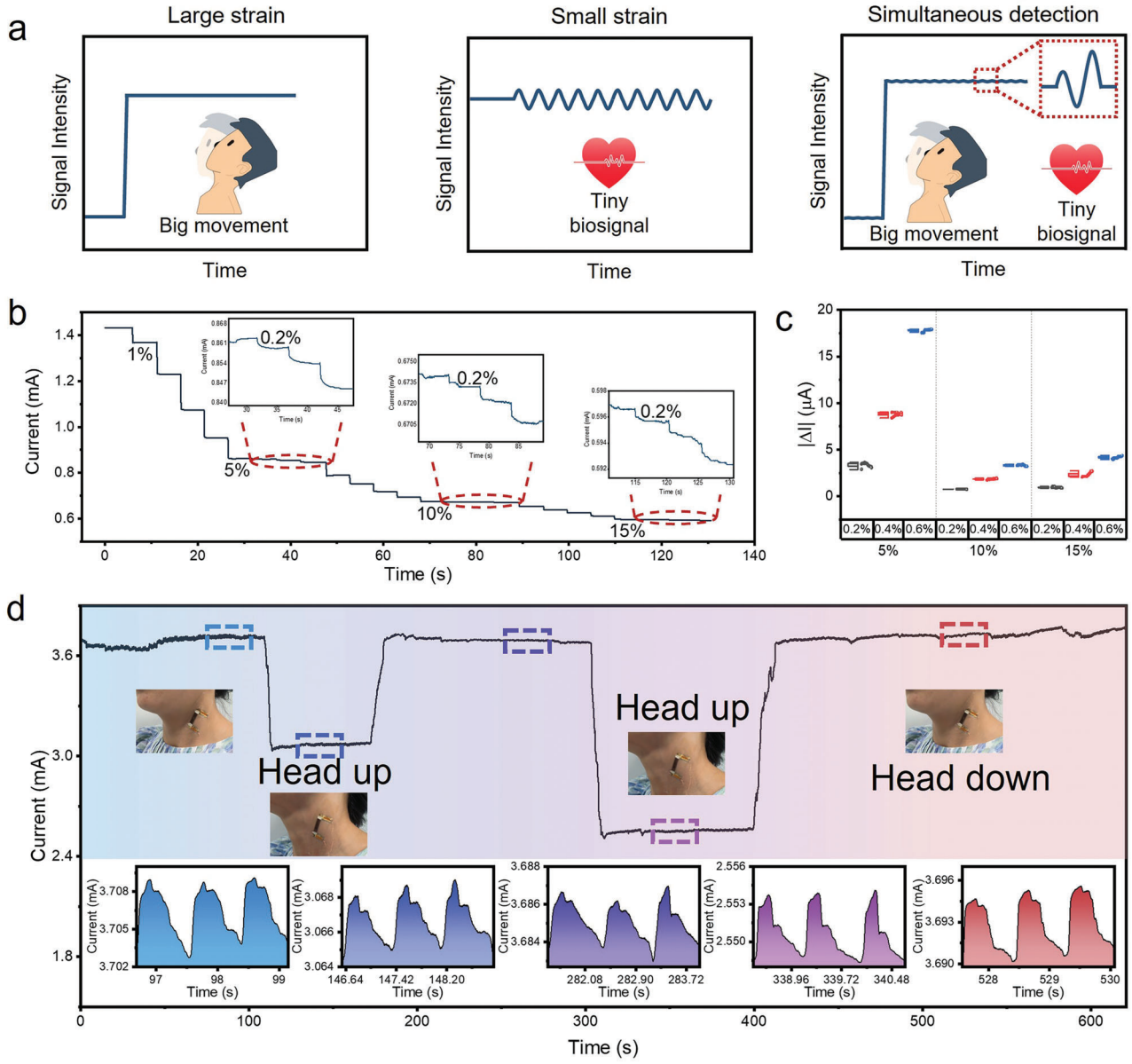

Figure 6. High resolution sensing performance of HSS based strain sensors. a) Schematic illustration of the response of the HSS based strain sensor to large and large, and simultaneous detection of small strain and large strain. b) Detection of tiny strain under different levels of loading strain. c) Statistic of the response of HSS based strain sensor to small strain under different levels of loading strain. d) Long-term carotid pulse monitoring during neck movement.

same time. The strain sensor based on our designed double conductive network hierarchical synergistic structure simultaneously possesses high sensitivity, broad sensing range, and high strain resolution, which is ideal for long-term health monitoring. Furthermore, to illustrate the ability of our HSS based sensors to simultaneously detect small pulse signals and large body movement signals, our sensor was attached to the volunteer's neck. The carotid pulse of the volunteer was stably and precisely recorded during neck movement for over ten minutes (Figure 6e). The three peaks of a typical human pulse waveform were stably recorded under different statuses, as shown in the lower part of Figure 6e. The above result demonstrates the potential application of our HSS based sensors in daily health monitoring.

3. Conclusion

In this work, we designed a hierarchical structure of Au micro cracks and CB nanoparticles which could enable synergistic effect and double conductive network. The synergistic deformation of the hierarchical structure of Au micro cracks and CB nanoparticles and the construction of double conductive network endowed the HSS based strain sensor with high sensitivity (GF = 2420), high strain resolution (0.2%), and broad detection

range of 45% strain. Further, we applied the HSS based strain sensor to monitor biosignals and body motions, which demonstrated the highly attractive potential for the application of personal healthcare, human-machine interfaces, and robotics. Our design of Au and CB hierarchical synergistic structure for strain sensors is a solid step toward the utilization of wearable systems.

4. Experimental Section

Fabrication of Self-Assembled CB Film: The CB nanoparticles (Chengdu Organic Chemistry Co., Ltd) were dispersed in ethanol with a concentration of 0.2 mg mL^{-1} by sonicating for 4 h. Then, the prepared CB dispersion was sprayed onto the surface of the water to form a highly uniform Langmuir monolayer film of loosely packed CB particles under the Marangoni forces and airflow. Subsequently, a sponge was placed at the edge of the container to quickly siphon water. Subsequently, the highly uniform Langmuir monolayer become closely packed toward the opposite direction of the siphon direction. Then the closely packed highly uniform monolayer CB films were transferred to a polystyrene substrate. Next, PDMS (Sylgard 184, Dow Corning) was stirred with the base and cure agent ratio of 10:1 and then spin-coated on the CB films. After PDMS was cured, the PDMS-CB was peeled off from the polystyrene substrate.

Fabrication of Strain Sensor: Then the PDMS-CB composite was cut into suitable sizes. Finally, a thin layer of gold was magnetron sputtered (PVD75 Kurt J. Lesker, Ar, 4 mTorr, 70 W) on the CB-PDMS film with different times. After that silver paste was used to connect copper wire and sensor for testing.

Measurements of Small Strain: After gold was magnetron sputtered, the Au-CB composite film was attached to commercial medical PU tape (Cofoe Medical Technology Co., Ltd) by soft silicone adhesive (JIAOSHUILAO, Guangdong Zhanlida novel materials Co., Ltd). After the silicone adhesive was cured, the strain sensor was attached to the volunteer's skin for muscle movement detection and pulse monitoring. The electrical response of strain sensors was recorded by Electrochemical workstation (Autolab PGSTAT302N Metrohm).

Characterization: The morphologies of Au film, CB film, and Au-CB composite were characterized using field-emission scanning electron microscopy (SU8020 Hitachi). The UV-Visible Spectrophotometer (UV-3600 SHIMADZU) was used to characterize the transmittance of CB films. The sensing performance and pulse monitor were tested using Electrochemical workstation (Autolab PGSTAT302N Metrohm) and home-made linear motor. The sound detection test was performed using oscilloscope (InfiniiVision MSOX4154A KEYSIGHT), and the STFT of the frequency spectrum was performed using Origin software.

Supporting Information

Supporting Information is available from the Wiley Online Library or from the author.

Acknowledgements

The authors thank the support of National Natural Science Foundation of China (No. 52125205, U20A20166 and 52192614), National key R&D program of China (2021YFB3200302 and 2021YFB3200304), Natural Science Foundation of Beijing Municipality (2222088), Shenzhen Science and Technology Program (Grant No. KQTD20170810105439418) and the Fundamental Research Funds for the Central Universities.

Conflict of Interest

The authors declare no conflict of interest.

Data Availability Statement

The data that support the findings of this study are available from the corresponding author upon reasonable request.

Keywords

flexible electronics, hierarchical structures, high resolution, long-term health monitoring, strain sensors

Received: February 21, 2023
Revised: March 29, 2023
Published online:

[1] L. Y. Duan, D. R. D'Hooge, L. Cardon, *Prog. Mater. Sci.* **2020**, *114*, 100617.
[2] S. Pyo, J. Lee, K. Bae, S. Sim, J. Kim, *Adv. Mater.* **2021**, *33*, 26.
[3] Y. W. Tan, X. H. Liu, W. Tang, J. Chen, Z. F. Zhu, L. Li, N. Zhou, X. Y. Kang, D. L. Xu, L. Wang, G. X. Wang, H. Tan, H. Li, *Adv. Mater. Interfaces* **2022**, *9*, 28.
[4] N. J. Douville, Z. Y. Li, S. Takayama, M. D. Thouless, *Soft Matter* **2011**, *7*, 6493.
[5] D. Kang, P. V. Pikhitsa, Y. W. Choi, C. Lee, S. S. Shin, L. F. Piao, B. Park, K. Y. Suh, T. I. Kim, M. Choi, *Nature* **2014**, *516*, 222.
[6] B. Park, J. Kim, D. Kang, C. Jeong, K. S. Kim, J. U. Kim, P. J. Yoo, T. i. Kim, *Adv. Mater.* **2016**, *28*, 8130.
[7] J. Li, R. R. Bao, J. Tao, M. Dong, Y. F. Zhang, S. Fu, D. F. Peng, C. F. Pan, *Appl. Phys. Rev.* **2020**, *7*, 9.
[8] Y. X. Li, T. Y. He, L. J. Shi, R. R. Wang, J. Sun, *ACS Appl. Mater. Interfaces* **2020**, *12*, 17691.
[9] M. Amjadi, M. Turan, C. P. Clementson, M. Sitti, *ACS Appl. Mater. Interfaces* **2016**, *8*, 5618.
[10] T. T. Yang, X. M. Li, X. Jiang, S. Y. Lin, J. C. Lao, J. D. Shi, Z. Zhen, Z. H. Li, H. W. Zhu, *Mater. Horiz.* **2016**, *3*, 248.
[11] S. Chen, Y. Wei, S. M. Wei, Y. Lin, L. Liu, *ACS Appl. Mater. Interfaces* **2016**, *8*, 25563.
[12] Z. Y. Liu, D. P. Qi, P. Z. Guo, Y. Liu, B. W. Zhu, H. Yang, Y. Q. Liu, B. Li, C. G. Zhang, J. C. Yu, B. Liedberg, X. D. Chen, *Adv. Mater.* **2015**, *27*, 6230.
[13] B. U. Hwang, J. H. Lee, T. Q. Trung, E. Roh, D. I. Kim, S. W. Kim, N. E. Lee, *ACS Nano* **2015**, *9*, 8801.
[14] G. H. Lim, N. E. Lee, B. Lim, *J. Mater. Chem. C* **2016**, *4*, 5642.
[15] M. R. Chen, W. F. Luo, Z. Q. Xu, X. P. Zhang, B. Xie, G. H. Wang, M. Han, *Nat. Commun.* **2019**, *10*, 9.
[16] H. Hwang, Y. Kim, J. H. Park, U. Jeong, *Adv. Funct. Mater.* **2020**, *30*, 11.
[17] W. Zhai, J. Zhu, Z. Wang, Y. Zhao, P. Zhan, S. Wang, G. Zheng, C. Shao, K. Dai, C. Liu, C. Shen, *ACS Appl. Mater. Interfaces* **2021**, *14*, 4562.
[18] K. N. Liu, J. S. Yu, Y. Li, X. W. Yan, D. Y. Bai, X. Q. Liao, Z. Q. Zhou, Y. Y. Gao, X. Yang, L. Li, *Adv. Mater. Technol.* **2019**, *4*, 7.
[19] F. Ershad, A. Thukral, J. Yue, P. Comeaux, Y. Lu, H. Shim, K. Sim, N. I. Kim, Z. Rao, R. Guevara, L. Contreras, F. Pan, Y. Zhang, Y. S. Guan, P. Yang, X. Wang, P. Wang, X. Wu, C. Yu, *ACS Appl. Mater. Interfaces* **2019**, *11*, 3823.
[20] J. W. Gao, Y. B. Fan, Q. T. Zhang, L. Luo, X. Q. Hu, Y. Li, J. C. Song, H. J. Jiang, X. Y. Gao, L. Zheng, W. Zhao, Z. H. Wang, W. Ai, Y. Wei, Q. B. Lu, M. Z. Xu, Y. T. Wang, W. T. Song, X. W. Wang, W. Huang, *Adv. Mater.* **2022**, *34*, 10.
[21] Y. Gao, F. Y. Guo, P. Cao, J. C. Liu, D. M. Li, J. Wu, N. Wang, Y. W. Su, Y. Zhao, *ACS Nano* **2020**, *14*, 3442.
[22] J. Lee, S. Pyo, D. S. Kwon, E. Jo, W. Kim, J. Kim, *Small* **2019**, *15*, 7.

[23] M. Z. Lin, Z. J. Zheng, L. Yang, M. S. Luo, L. H. Fu, B. F. Lin, C. H. Xu, *Adv. Mater.* **2022**, *34*, 13.
[24] T. S. D. Le, J. N. An, Y. Huang, Q. Vo, J. Boonruangkan, T. Tran, S. W. Kim, G. Z. Sun, Y. J. Kim, *ACS Nano* **2019**, *13*, 13293.
[25] K. C. Xu, Y. Fujita, Y. Y. Lu, S. Honda, M. Shiomi, T. Arie, S. Akita, K. Takei, *Adv. Mater.* **2021**, *33*, 13.
[26] Y. Park, J. Shim, S. Jeong, G.-R. Yi, H. Chae, J. W. Bae, S. O. Kim, C. Pang, *Adv. Mater.* **2017**, *29*, 1606453.
[27] H. C. Wang, R. C. Zhou, D. H. Li, L. R. Zhang, G. Z. Ren, L. Wang, J. H. Liu, D. Y. Wang, Z. H. Tang, G. Lu, G. Z. Sun, H. D. Yu, W. Huang, *ACS Nano* **2021**, *15*, 9690.
[28] J. H. Pu, X. Zhao, X. J. Zha, W. D. Li, K. Ke, R. Y. Bao, Z. Y. Liu, M. B. Yang, W. Yang, *Nano Energy* **2020**, *74*, 11.
[29] I. You, D. G. Mackanic, N. Matsuhisa, J. Kang, J. Kwon, L. Beker, J. Mun, W. Suh, T. Y. Kim, J. B. H. Tok, Z. N. Bao, U. Jeong, *Science* **2020**, *370*, 961.
[30] D. Y. Choi, M. H. Kim, Y. S. Oh, S. H. Jung, J. H. Jung, H. J. Sung, H. W. Lee, H. M. Lee, *ACS Appl. Mater. Interfaces* **2017**, *9*, 1770.
[31] B. Chen, Y. D. Cao, Q. Y. Li, Z. Yan, R. Liu, Y. J. Zhao, X. Zhang, M. Y. Wu, Y. X. Qin, C. Sun, W. Yao, Z. Y. Cao, P. M. Ajayan, M. O. L. Chee, P. Dong, Z. F. Li, J. F. Shen, M. X. Ye, *Nat. Commun.* **2022**, *13*, 12.
[32] Q. S. Li, G. Chen, Y. J. Cui, S. B. Ji, Z. Y. Liu, C. J. Wan, Y. P. Liu, Y. H. Lu, C. X. Wang, N. Zhang, Y. Cheng, K. Q. Zhang, X. D. Chen, *ACS Nano* **2021**, *15*, 9955.
[33] S. H. Peng, S. Y. Wu, Y. Y. Yu, P. Blanloeuil, C. H. Wang, *J. Mater. Chem. A* **2020**, *8*, 20531.
[34] Y. D. Horev, A. Maity, Y. B. Zheng, Y. Milyutin, M. Khatib, M. M. Yuan, R. Y. Suckeveriene, N. Tang, W. W. Wu, H. Haick, *Adv. Mater.* **2021**, *33*, 9.
[35] Y. F. Hu, T. Q. Huang, H. J. Lin, L. W. Ke, W. Cao, C. Chen, W. Q. Wang, K. Rui, J. X. Zhu, *J. Mater. Chem. A* **2022**, *10*, 928.
[36] D. K. Wang, J. Q. Zhang, G. L. Ma, Y. Q. Fang, L. P. Liu, J. X. Wang, T. Sun, C. C. Zhang, X. C. Meng, K. J. Wang, Z. W. Han, S. C. Niu, L. Q. Ren, *ACS Nano* **2021**, *15*, 19629.
[37] Q. Y. Duan, B. J. Lan, Y. Lv, *ACS Appl. Mater. Interfaces* **2022**, *14*, 1973.
[38] X. Y. He, Y. N. Hao, M. T. He, X. H. Qin, L. M. Wang, J. Y. Yu, *ACS Appl. Mater. Interfaces* **2021**, *13*, 60498.
[39] S. L. Zhu, H. Y. Sun, Y. Lu, S. L. Wang, Y. Y. Yue, X. W. Xu, C. T. Mei, H. N. Xiao, Q. L. Fu, J. Q. Han, *ACS Appl. Mater. Interfaces* **2021**, *13*, 59142.
[40] X. C. Tan, J. D. Xu, J. M. Jian, G. H. Dun, T. R. Cui, Y. Yang, T. L. Ren, *ACS Nano* **2021**, *15*, 20590.
[41] S. Y. Wu, S. H. Peng, Z. J. Han, H. W. Zhu, C. H. Wang, *ACS Appl. Mater. Interfaces* **2018**, *10*, 36312.
[42] S. W. Pan, Z. Y. Liu, M. Wang, Y. Jiang, Y. F. Luo, C. J. Wan, D. P. Qi, C. X. Wang, X. Ge, X. D. Chen, *Adv. Mater.* **2019**, *31*, 8.
[43] J. H. Lee, J. Kim, D. Liu, F. M. Guo, X. Shen, Q. B. Zheng, S. Jeon, J. K. Kim, *Adv. Funct. Mater.* **2019**, *29*, 1901623.
[44] H. Zhang, D. Liu, J. H. Lee, H. M. Chen, E. Kim, X. Shen, Q. B. Zheng, J. L. Yang, K. Y. Kim, *Nano-Micro Lett.* **2021**, *13*, 15.
[45] J. J. Pan, B. W. Hao, W. F. Song, S. X. Chen, D. Q. Li, L. Luo, Z. G. Xia, D. S. Cheng, A. C. Xu, G. M. Cai, X. Wang, *Compos. Pt. B-Eng.* **2020**, *183*, 107683.
[46] E. Lee, T. Kim, H. Suh, M. Kim, P. V. Pikhitsa, S. Han, J. S. Koh, D. Kang, *Sensors* **2018**, *18*, 8.
[47] N. E. Jansson, Y. Leterrier, J. A. E. Manson, *Eng. Fract. Mech.* **2006**, *73*, 2614.